RSC Advances

PAPER

View Article Online
View Journal | View Issue

Cite this: *RSC Adv.*, 2025, **15**, 2779

Hierarchical structures of GO-supported BiBTC MOFs for efficient RhB photodegradation

Van Cuong Nguyen, *[a] Trinh Duy Nguyen, [b] Qui Thanh Hoai Ta [c] and Ai Le Hoang Pham *[a]

Received 25th November 2024
Accepted 18th January 2025

DOI: 10.1039/d4ra08337g

rsc.li/rsc-advances

This study, we synthesized a graphene oxide@BiBTC MOF (GO@BiBTC) photocatalyst *in situ* using a hydrothermal method. The resulting samples were comprehensively characterized using FT-IR, Raman spectra, XRD, SEM, TEM, XPS and UV-Vis spectroscopy. The photodegradation reaction fits the pseudo-first-order kinetics and the deterioration rate constants (k) value of BiBTC, GO@BiBTC MOF composites were 0.03 and 0.07 min^{-1}, respectively. The GO@BiBTC MOF composite demonstrated a reduced energy band gap compared to BiBTC, with values of 3.39 eV and 3.6 eV, respectively. Among the various samples, the optimized GO@BiBTC MOF demonstrated superior photocatalytic performance, achieving a 98% degradation rate of rhodamine B (RhB) within 60 min, outperforming the pure BiBTC MOF. The significantly enhanced photocatalytic activity of BiBTC@GO can be attributed to its enhanced charge transfer and adsorption-(photo) degradation. Furthermore, the outstanding photo-stability of the GO@BiBTC MOF photocatalyst was investigated by conducting recycling measurements consecutively over five cycles for RhB with 90% photodegrading efficiency.

Introduction

Nowadays, the demand for potable water is steadily increasing due to rapid population growth and significant industrial activities. However, the substantial contamination of natural water resources, resulting from various industrial discharges, domestic effluents, and medical waste, has severely restricted access to clean water.[1–3] Particularly, the excessive discharge of organic pollutants significantly contributes to overall water pollution. Hence, it is imperative to find effective methods to address this global environmental challenge.[4]

In recent years, photocatalytic treatment using metal oxide semiconductors has garnered considerable interest from researchers due to its appealing characteristics, such as ease of use, high efficiency, safety, and environmental friendliness. Indeed, numerous semiconductor-based photocatalytic catalysts have been studied for sustainable improvements in photocatalytic treatment.[5–7]

Metal–organic frameworks (MOFs) have emerged as potential materials among various metal oxides due to their strong dispersibility, well-defined porous structure, narrow band gap energy, high surface area, and stability.[8,9] However, MOF materials suffer from disadvantages such as poor separation, limited light-harvesting capacity, and low photocarrier transfer efficiency inherent to their properties. To address these drawbacks, composite MOFs have been developed, including MOF/carbon composites, MOF/metal nanoparticle composites, and MOF/metal oxide composites.[10] In addition to the aforementioned MOFs, Bi-MOFs incorporating 1,3,5-benzenetricarboxylic acid (H_3BTC) and bismuth metal represent promising candidates for constructing high specific surface area Bi-based materials.[11,12]

Transition metals like bismuth are of significant interest in various fields, particularly in energy storage and catalysis, due to their high theoretical capacities. This refers to their ability to store or process a large amount of charge or energy in comparison to other materials. Bismuth, a key semi-metallic element, exhibits several unique physical properties that make it an exemplary material in the fields of materials science and physics. The presence of a hole pocket and an electron pocket in the valence band and conduction band, respectively, across the Fermi level, contributes to the distinctive semi-metallic characteristics of bismuth. Additionally, bismuth is recognized for being environmentally friendly, non-toxic, and relatively affordable compared to precious metals. Moreover, many MOF materials derived from bismuth have been reported. The Bi^{3+} cation can form bonds with numerous surrounding atoms or groups, allowing it to form polycrystals. Moreover, the Bi^{3+} ion can exhibit various coordination numbers and different coordination geometries (such as triangular, tetrahedral, hexagonal, *etc.*), facilitating the creation of complex structures.

[a]*Faculty of Chemical Engineering, Industrial University of Ho Chi Minh City, No. 12 Nguyen Van Bao Street, Ward 1, Go Vap District, Ho Chi Minh City, Vietnam. E-mail: nvc@iuh.edu.vn; phamhoangaile@iuh.edu.vn*

[b]*Institute of Applied Technology and Sustainable Development, Nguyen Tat Thanh University, Ho Chi Minh City, Vietnam*

[c]*Institute of Chemical Technology, Vietnam Academy of Science and Technology, 1A TL29 Street, Thanh Loc Ward, District 12, Ho Chi Minh City, Vietnam*

Bismuth-based MOFs demonstrate good catalytic potential due to the presence of multiple insoluble metal sites.[13–15]

Michelle and colleagues developed a novel Bi-MOF-based structure, UU-200 (Uppsala University), with high specific surface areas (141 $m^2 g^{-1}$) for CO_2 and SF_6 adsorption at room temperature.[16] The UU-200 features an orthorhombic unit cell (a = 2.251 nm, b = 2.753 nm, and c = 1.042 nm) with *Pnnm* space group (# 58). Continuous rotation electron diffraction results indicate that UU-200 possesses large pore size structures (0.34–0.35 nm), making it suitable for greenhouse gas adsorbents with high-efficiency uptake capacities.[16]

Graphene oxide (GO) has been explored as an efficient adsorbent in the field of adsorption due to its highly porous structure and environmentally friendly properties.[17–19] GO can be easily prepared from natural graphite and dispersed well in polar solvents owing to its hydrophilic character.[20] The functional groups (hydroxy, epoxy, and carbonyl) on GO nanosheets provide a favorable basis for the formation of GO/MOF composites.[21–23]

Combining inorganic semiconductors or metallic materials to build composites has been shown to improve the photocatalytic performance of MOFs, exemplified by BiOBr@Bi-MOF,[24] $BiVO_4$@α-Fe_2O_3,[25] MIL-125(Ti)/Bi_2WO_6 (ref. 26) and others. Nguyen and colleagues demonstrated that the Ag–Zn–BTC/GO composite exhibited enhanced photocatalytic performance in the removal of reactive yellow 145 dye from wastewater, attributed to improved carrier separation efficiency and an increased specific surface area (1626 $m^2 g^{-1}$).[27] Similarly, Vu *et al.* reported the preparation of Fe–BTC/GO heterostructures *via* the microwave-assisted method and subsequent hydrothermal treatment, resulting in improved photocatalytic performance in the degradation of reactive yellow 145. The optimal composite achieved a 98% removal efficiency after 1 h of light exposure, which can be attributed to the increased surface area and energy band gap of the heterojunction composite.[28]

Rhodamine B (RhB) is a chemical compound as a dye, which is used in industries and pharmaceutical products. However, when released into the environment, RhB adversely affects the habitat of aquatic organisms. Furthermore, the prolonged accumulation of RhB in the human body could potentially cause serious health issues, including allergies, itching, coughing, and chest pain. Due to these harmful effects, effective measures are necessary to remove RhB from wastewater to protect both human health and natural environment. The treatment of RhB in wastewater is essential and important. Depending on the concentration of RhB, the composition of the wastewater, the required output quality, and actual conditions, various methods can be employed to treat RhB in wastewater. Several methods have been researched and applied to treat rhodamine B in wastewater, including biological methods, adsorption methods, and advanced oxidation processes (AOP).[29–31]

Photocatalysis is considered an effective solution to the problem of environmental pollution.[32,33] This process harnesses light energy to stimulate a catalyst capable of oxidizing or reducing rhodamine B to fewer toxic substances. Pham and colleagues synthesized a Bi-based MOF from a bismuth metal center and linker H_3BTC, forming MIX-UCAU17 composite.[34] Degradation experiments with the prepared MIX-UCAU photocatalyst demonstrated a high photodegradation efficiency of approximately 99% within 90 minutes under LED light irradiation. Zhu *et al.* developed a 2D BiOBr MOF based on Bi CAU-17 using a facile solvent thermal transformation method.[35] The BiOBr/CAU-17-2 h photocatalyst exhibited enhanced photocatalytic activity for RhB degradation (20 mg L^{-1}, 50 min).

Considering their complementary band structures and advantages, the combination of GO and Bi-MOF can yield an effective composite photocatalyst with a high specific surface area, efficient charge separation, and high transfer efficiency.[36] These outstanding characteristics of MOF-based photocatalysts position them as promising candidates for organic pollutant degradation through photocatalytic activity.

In this study, we conducted an elegant synthesis of an *in situ* Bi-based MOF on GO heterojunction catalyst to enhance photocatalytic activity. GO@BiBTC MOF photocatalyst was successfully synthesized using the hydrothermal technique with varying ratios of GO and BiBTC. The optimal catalyst demonstrated superior photocatalytic activity compared to pure Bi-based MOF. The adsorption-photocatalytic performance of the composite was assessed for its ability to adsorb and photodegrade rhodamine B pollutants in wastewater. Additionally, a proposed mechanism was investigated to elucidate the outstanding photocatalytic performance of the hybrid structures.

Experimental

Materials and chemicals

Bismuth(III) nitrate pentahydrate ($Bi(NO_3)_3 \cdot 5H_2O$, 98.0%), benzene-1,3,5-tricarboxylic acid (H_3BTC, 98.0%), *tert*-butanol (*t*-BuOH, 99.5%), rhodamine B (95%), and 1,4-benzoquinone (99%) were sourced from Sigma-Aldrich. *N*,*N*-Dimethylformamide (DMF, 99%), methanol (MeOH, 99.5%), sodium oxalate (99.8%), and potassium dichromate (99.8%) were purchased from Xilong Scientific Co., Ltd. All the chemicals were used as received.

Synthesis of GO, BiBTC, and BiBTC@GO

Graphene oxide (GO) was synthesized using a modified Hummers' method.[37] Specifically, 3 g of graphite flakes were gradually added to 400 mL of concentrated H_2SO_4/H_3PO_4 acid mixture (9 : 1) and stirred vigorously for one hour. Subsequently, 18 g of $KMnO_4$ was added to the mixture, which was maintained at 30 °C for 72 h before introducing 17 mL of H_2O_2 (30%) to the reaction solution. The obtained filtrate is rinsed several times with 0.1 M HCl and deionized (DI) water to ensure complete acid removal. The yellow-brown residual powder is then washed with warm water up to three times to eliminate any remaining impurities. The final product was dried at 60 °C for 48 h.

In situ prepare of GO@BiBTC MOF heterostructures was performed by one-step hydrothermal technique, as shown in Scheme 1. In a typical step, a different amount of GO (20, 50, 80 mg) was well dispersed in DMF (10 mL) for 10 min using sonication system (solution I). A 0.1495 g of $Bi(NO_3)_3 \cdot 5H_2O$, 0.7291 g H_3BTC dissolved in 30 mL of DMF, and 30 mL of CH_3OH with constant stirring (solution II).[38] After that, the solution I was poured into solution II under a magnetic stirring

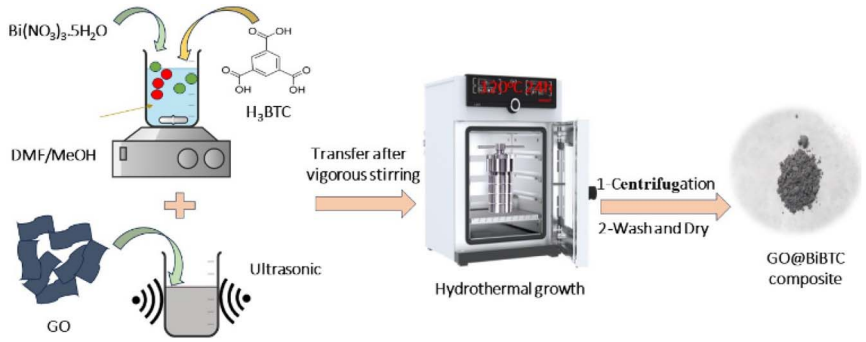

Scheme 1 The presentation of the synthesis of the GO@BiBTC MOF heterostructures.

at 5000 rpm to guarantee that the precursors were well-dispersed. Thereafter, the mixture transferred into a 100 mL Teflon lined stainless steel autoclave reactor and subjected to keep in an oven at 120 °C for 24 h.

The reaction mixture was cooled down to room temperature and reaction solution was collected through centrifugation to get product. The resulting powder was washed three times with distilled water, DMF, and methanol to remove by-products, then dried overnight at 80 °C in a vacuum oven. Finally, the GO@BiBTC composites were designated as GO1@BiBTC, GO2@BiBTC, GO3@BiBTC, respectively. Pure BiBTC was prepared in same manner for comparison but without GO.

Photocatalytic measurements

The photocatalytic activity of the as-synthesized samples was carefully evaluated by the deterioration of the RhB solution under simulated solar light irradiation. A 40 W LEDS with size of 3.45 mm × 3.45 mm × 2.36 mm and with an intensity of 141 W m^{-2} (Cree, Inc., Durham, NC, USA) lamp was utilized as light source. The photocatalytic was conducted in a 250 mL Lab Double layer jacket glass beaker. The beaker was place in dark box cover with aluminum foil and the temperature was maintained at room temperature by a cooling jacket. For this measurement, 10 mg of photocatalyst was well-dispersed into 50 mL of RhB (15 mg L^{-1}) in 250 mL Lab Double layer jacket glass beaker. This result mixture was kept in dark environment for 1 h to establish the equilibrium phase at room temperature. After that, this mixture solution was irradiated under simulated solar light irradiation for 60 min. 5 mL of reaction solution was collected and analyzed through UV-Vis system at the illumination time interval of 15 min. The experiments were performed three times.

Radical species trapping experiment

To confirm the effect of major species in the removal of RhB, 1,4-benzoquinone (BQ, 1.0 mM), sodium oxalate ($Na_2C_2O_4$, 10 mM), potassium dichromate ($K_2Cr_2O_7$, 10 mM), tributylamine (TBA, 10 mM) were used as similar as the photodegradation experiment. The experiments were performed three times.

Characterization

For Fourier-transform infrared (FT-IR) spectroscopy measurements, the prepared samples were mixed with KBr and

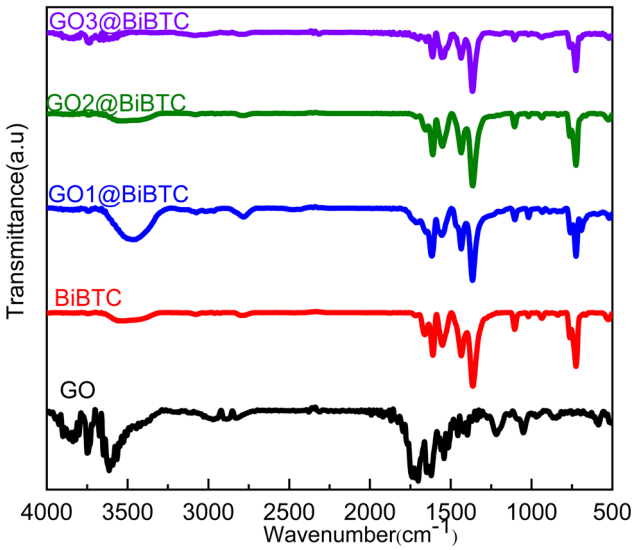

Fig. 1 FT-IR spectra of the as-synthesized samples.

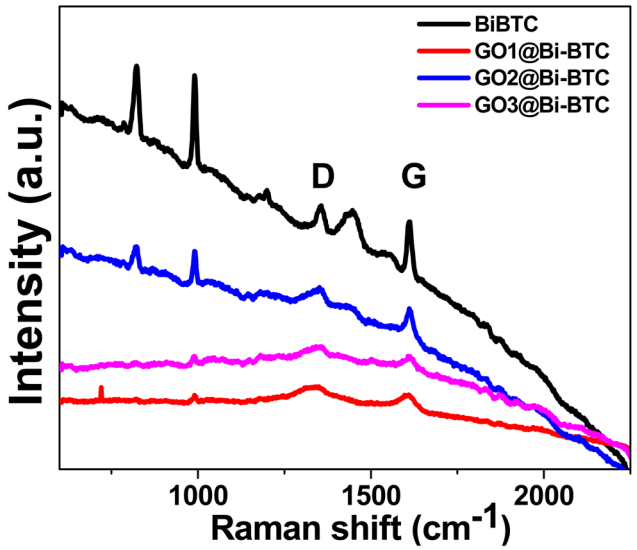

Fig. 2 Raman spectra of the as-synthesized samples.

compressed into KBr pellets using a hydraulic press. The FT-IR spectra were recorded with a Bruker Tensor 27 spectrometer (Germany) over a scanning wavenumber range of 400–4000 cm^{-1}. The morphology of the composite was examined using a field emission scanning electron microscope (JSM-IT800, Tokyo, Japan) equipped with an energy-dispersive X-ray microanalyzer H-7593 (Horiba, Japan). X-ray diffraction (XRD) analysis was performed on a LabX XRD-6100 (Shimadzu, Japan) with Cu-Kα radiation, scanning from 5° to 75° in 2θ increments. The UV-visible diffuse reflectance spectra of the materials were obtained using a Cary UV-Vis 4000 spectrophotometer, while ultraviolet-visible spectroscopy was carried out with a Cary 3500 UV-Vis spectrophotometer. Thermogravimetric analysis (TGA) of samples were measured on the TGA 550 (TA Instruments, US). Photoluminescence (PL) spectra were measured using a Cary Eclipse Fluorescence Spectrometer (Agilent) with an excitation wavelength of 400 nm.

Electrochemical Impedance Spectroscopy (EIS) was conducted through Nyquist plots using an AUTOLAB-PGSTAT204 (Metrohm, Netherlands) with a three-electrode configuration. The working electrodes were prepared by mixing 10 mg of the material with 20 μL of Nafion, followed by adding 1 mL of an ethanol and water solution. This suspension was then spray-coated onto ITO-coated glass substrates. A 0.5 M Na_2SO_4 solution was used as the electrolyte to provide a stable conductive environment between the electrodes throughout the experiment.

LC-MS analysis was performed to determine the compositions in the reaction solution using liquid chromatography coupled with an ion trap detector on a Thermo Finnigan LCQ MS system (Agilent 6410 Triple Quad LC/MS/MS). The conditions included a C18 reverse-phase column, a mobile phase of methanol and water (1 : 1, v/v), a flow rate of 0.5 mL min^{-1}, and an injection volume of 50 μL.

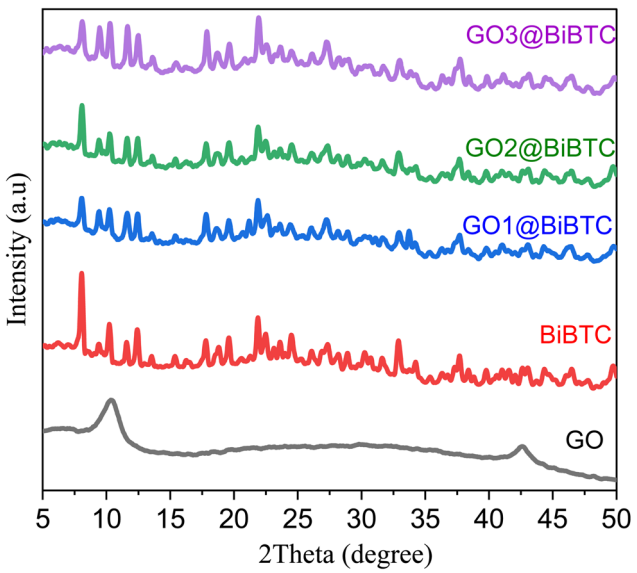

Fig. 3 XRD patterns of the as-synthesized samples.

Results and discussion

Fabrication and characterization of photocatalyst

Fig. 1 illustrates FT-IR spectra of pure GO, BiBTC, and composites, where for BiBTC, the analyzed absorption peaks at 3521 cm^{-1} and 1549–1365 cm^{-1} are credited to O–H stretching vibrations and –COO carboxylate groups, respectively. For GO, C–O stretching vibrations appear at 608 cm^{-1}. The C=C vibrations in aromatic rings appear at 1639 cm^{-1}, while C=O in carboxyl groups is located at 1728 cm^{-1}. The peak owing to the O–H deformation is located at 3634–3853 cm^{-1}, while ether groups with C–O–C stretch appear at 2833–2966 cm^{-1}.[39,40] In the case of GO@BiBTC MOF photocatalysts, the FT-IR spectrum displays all the characteristic peaks of both pure GO and BiBTC with a small intensity of peak position, ascribing the difference in weight ratio of the two components. There is no peak

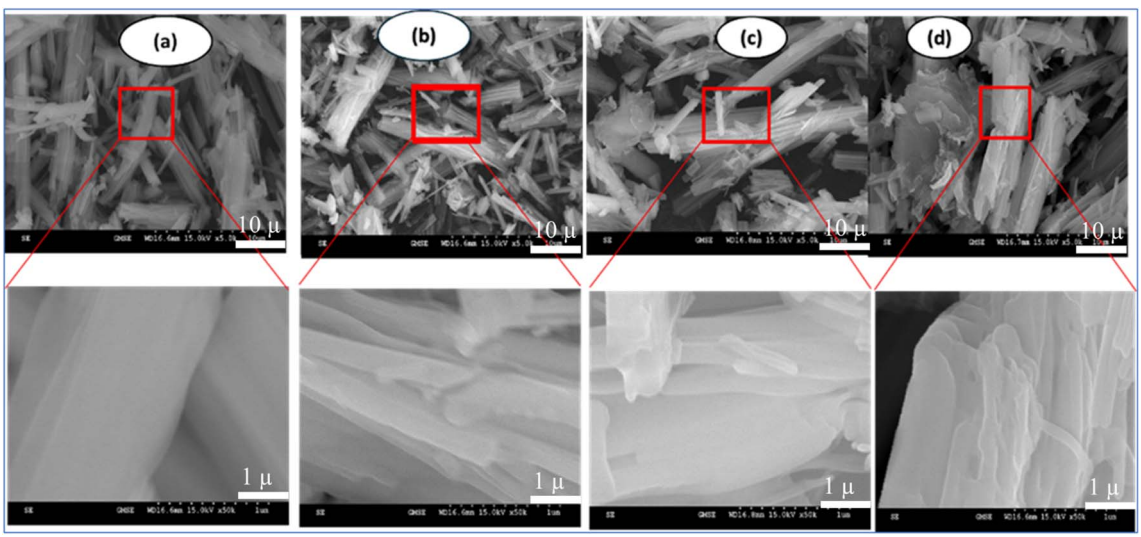

Fig. 4 SEM micrographs of the as-synthesized samples (a) BiBTC, (b) GO1@BiBTC MOF, (c) GO2@BiBTC MOF, (d) GO3@BiBTC MOF photocatalysts.

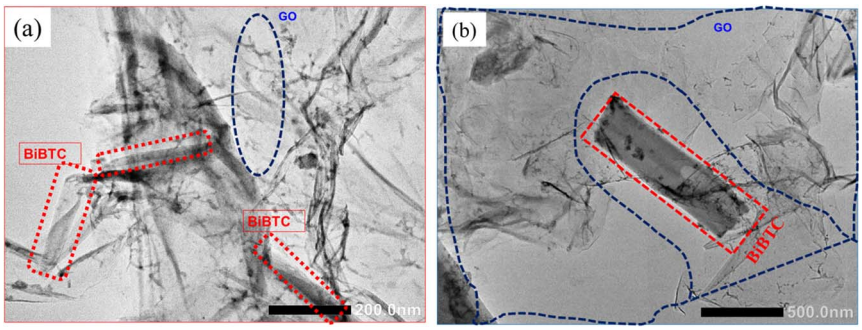

Fig. 5 TEM image of GO2@BiBTC MOF photocatalysts (a) scale bar 200 nm and (b) scale bar 500 nm.

absorbance at 1200 cm^{-1} can be supplementary with Bi–O stretch of BiO_2 destroyed in the case of composites.

Fig. 2 displays the Raman spectra of the as-synthesized sample. The peaks observed around 1600 cm^{-1} and 1325 cm^{-1} correspond to the C sp^2 and sp^3 bonds, respectively, which can be attributed to the graphitic (G) bands and characteristic defects (D). It is apparent that the relative intensity of the D-band is lower than that of the G-band, indicating graphitization and the introduction of more defects. The peaks at 800–1000 cm^{-1} are attributed to the C–H and C–C functional groups.[41–43]

The crystal structure of all the photocatalysts was analyzed by XRD as displayed in Fig. 3. The XRD pattern of GO (black line) appears in intensive peaks at $2\theta = 10.5°$ and 42.3° corresponding to (001) and (100) planes indicate the formation of graphite oxide structure.[44] The XRD pattern of BiBTC and composites shows predominant diffraction peaks at $2\theta \sim 8.2°$, 9.8°, 12.5°, 17.9°, 21.7°, 24.5°, 32.1° and 37.5°, which are consistent with the simulated pattern and the characteristics of the CAU-17 and UU-200 frameworks (CCDC 2103784).[16] Interestingly, the GO@BiBTC MOF photocatalysts reveals all the multiple sharp XRD peaks for both Bi-based MOF and GO without slight shifts in their position. No foreign phase was recorded, indicating that the prepared photocatalysts is of high purity.

The morphologies of as-synthesized samples were characterized using SEM. As shown in Fig. 4a, BiBTC have rod-like structures with an average size of around 400 nm. For the composite, rod-like BiBTC was scattered in the coarse GO. GO@BiBTC MOF photocatalyst seems to be a layer-by-layer structure, which sandwiched layers between BiBTC and GO architecture (Fig. 4b–d). These folded morphologies enable GO@BiBTC MOF heterostructure larger surface area, helping to boost the adsorption/photocatalytic capacity of RhB. Additionally, the TEM image presented in Fig. 5 reveals that the surface of the GO@BiBTC composite is rough, featuring thin,

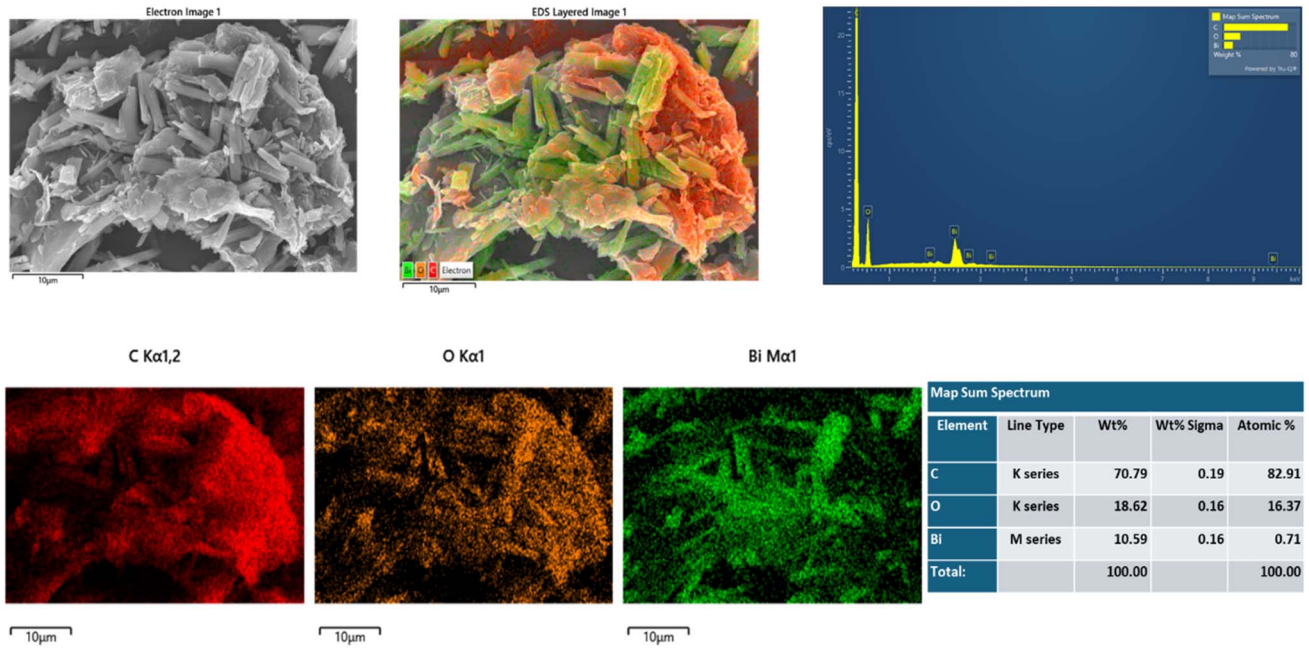

Fig. 6 SEM and EDS analysis of GO2@BiBTC MOF photocatalysts.

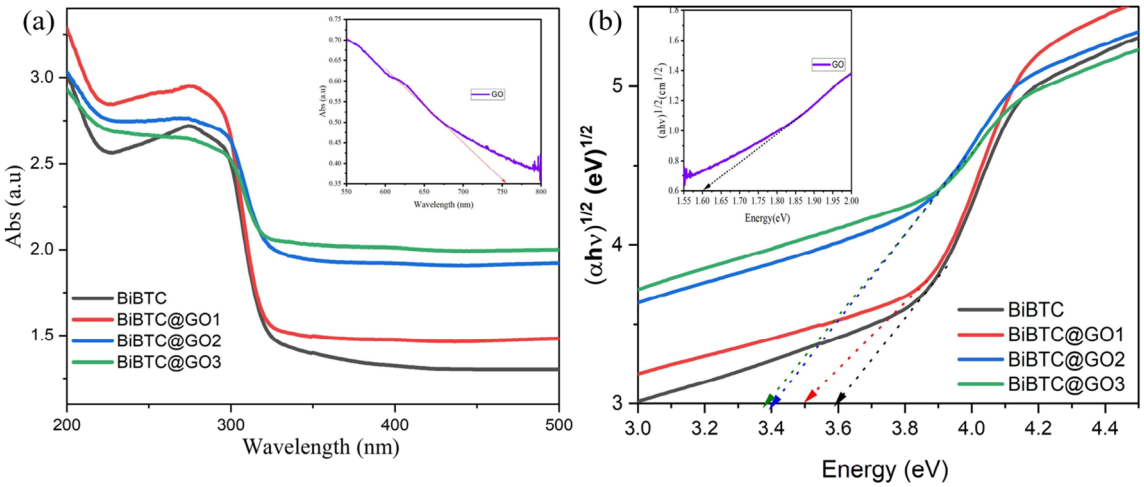

Fig. 7 (a) UV-Vis spectra and (b) the Tauc plots of the as-synthesized samples.

transparent, layered wrinkles of GO and condensed, rod-like bundles of BiBTC.

Furthermore, elemental mappings of selected GO2@BiBTC, as depicted in Fig. 6, confirm the presence and distribution of C, Bi, and O in the composite. The experimental results presented herein demonstrate the successful preparation of GO@BiBTC, consistent with the characterization findings from FTIR and XRD analyses.

Fig. 7 illustrates absorption spectra of pure BiBTC, and GO@BiBTC MOF composites with different weight ratio. The absorption threshold of pure BiBTC (green line) is observed at 325 nm. In contrast, GO@BiBTC MOF exhibits enhanced absorption compared to BiBTC specifically in the 330–360 nm range. This indicates that all GO@BiBTC MOF composites demonstrate stronger optical absorption across the entire UV and visible spectrum compared to pure BiBTC. The improved optical absorption potentially facilitates the capture of a greater number of photons, leading to increased generation of photo-induced carriers.[45,46] The bandgap (E_g) values were obtained from the direct application of the Tauc plot method.[47] According to the Tauc equation, the energy band gap of BiBTC, GO1@BiBTC MOF, GO2@BiBTC MOF and GO3@BiBTC MOF were calculated around 3.6 eV, 3.5 eV, 3.4 eV and 3.39 eV, respectively. The extensively lowered optical band gap of the photocatalyst indicates its better photo performance than bare counterparts.

The TGA analysis results of the materials, shown in Fig. 8 indicated that GO exhibits low thermal stability. Between 100–350 °C, its mass significantly decreased from 89% to 43.8%, due to the decomposition of organic functional groups on the GO structure, such as –OH, –COOH, and epoxy. Beyond 350 °C, the mass loss attributed to the degradation of the carbon structure. For BiBTC, the main mass loss occurred between 300–400 °C, corresponding to the decomposition of functional groups

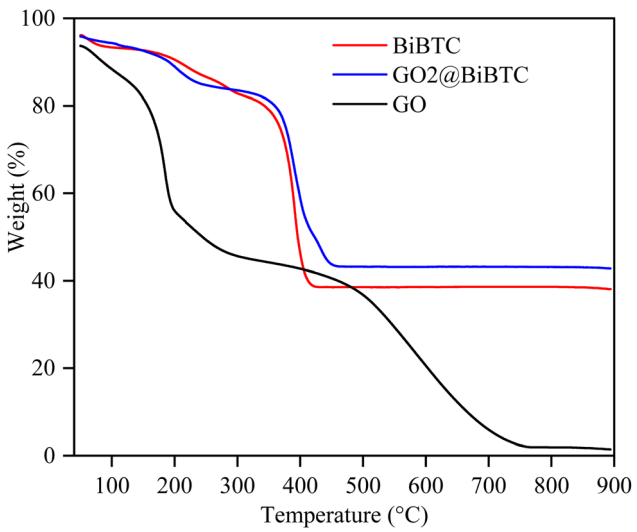

Fig. 8 TGA analyses of the as-synthesized samples.

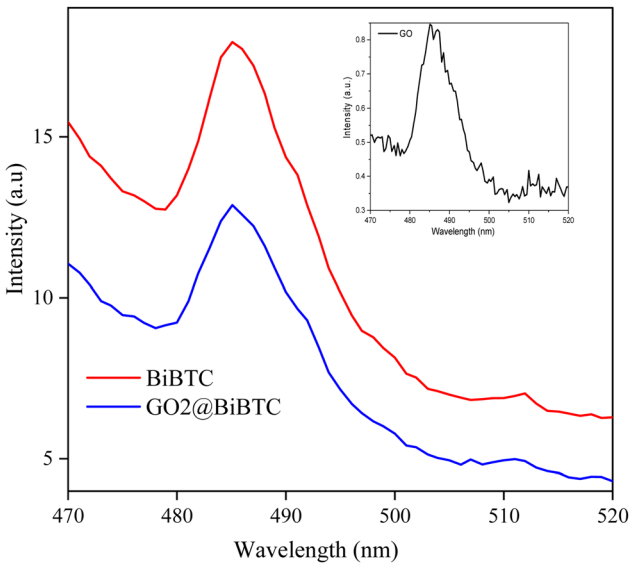

Fig. 9 Photoluminescence spectra of the as-synthesized samples.

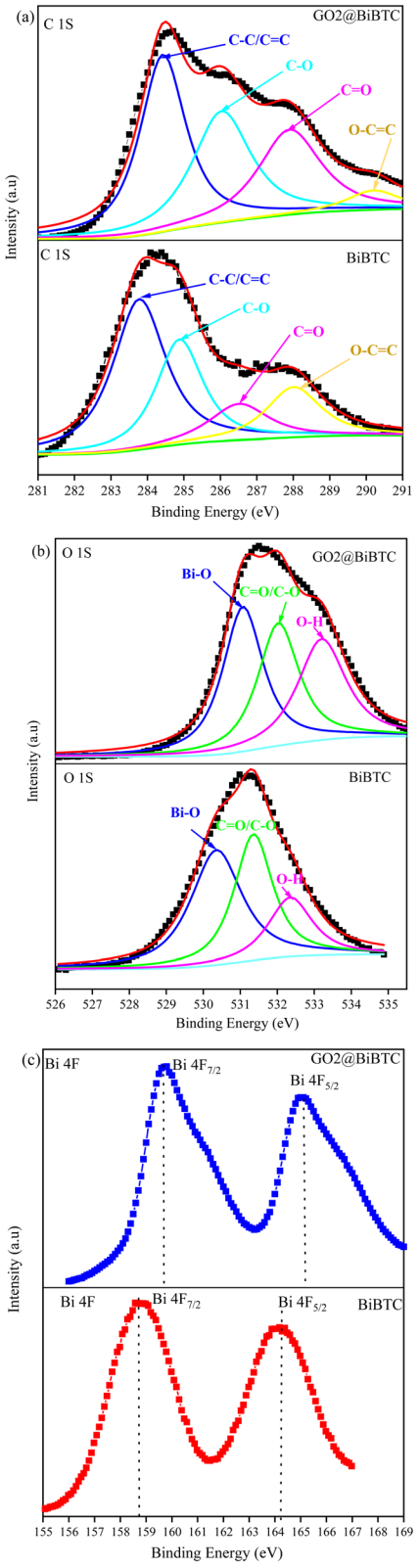

Fig. 10 XPS spectrum of BiBTC and GO@BiBTC with signals of (a) C 1s, (b) O 1s, and (c) Bi 4f.

within the metal–organic framework. The GO@BiBTC composite demonstrated higher thermal stability compared to standalone GO and BiBTC, owing to the interactions between

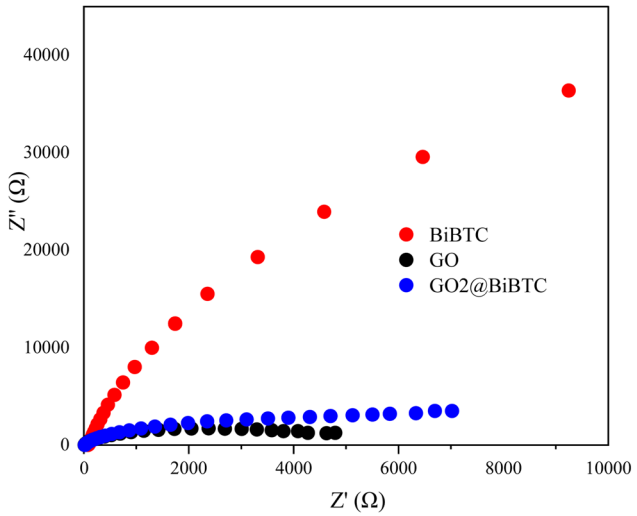

Fig. 11 EIS Nyquist plots of spectra of the as-synthesized samples.

GO and BiBTC, which significantly enhance the thermal resistance of materials.

Photoluminescence (PL) spectroscopy demonstrates that the recombination of photo-induced electron–hole pairs under UV or visible light irradiation leads to photon emission, manifesting as characteristic PL peaks. In the GO@BiBTC composite, the integration of GO substantially diminishes the PL intensity of the BiBTC metal–organic framework, as depicted in Fig. 9. This attenuation is attributed to GO's exceptional electron transport properties, which effectively suppress electron–hole recombination, thereby enhancing the photocatalytic degradation of organic contaminants.[48]

The XPS spectra provide information on the chemical composition and binding energies of atoms on the surface of BiBTC and GO@BiBTC materials. The C 1s peak of the material (Fig. 10a) displays binding energy peaks of BiBTC at 283.78 eV, 284.88 eV, 286.58 eV, and 288.8 eV, corresponding to C=C/C–C, C–O, C=O, and O–C=O bonds of BiBTC, respectively. However, the binding energy peaks for C–C/C=C, C–O, C=O, and O–C=O of the GO@BiBTC composite are shifted to 284.5 eV, 286.1 eV, 288.1 eV, and 290.3 eV, respectively. This result demonstrates that the interaction between GO and BiBTC alters the chemical environment around the carbon atoms. Additionally, the O 1s peak of BiBTC can be deconvoluted into three main peaks corresponding to the functional groups: Bi–O at 530.38 eV, the carboxylate groups of the BTC linkers at 531.38 eV, and OH at 532.38 eV. For the GO@BiBTC composite, the binding energy positions of the Bi–O, the carboxylate groups of the BTC linkers, and O–H groups shift to 531.1 eV, 532.1 eV, and 533.2 eV, respectively, reflecting the interaction between GO and the BiBTC (Fig. 10b). The binding energy values of the Bi 4f spectra for BiBTC are determined to be 158.78 eV (Bi $4f_{7/2}$) and 164.38 eV (Bi $4f_{5/2}$), with a binding energy difference (ΔE) between Bi $4f_{5/2}$ and Bi $4f_{7/2}$ of 5.3 eV. In the GO@BiBTC composite, the interaction between GO and BiBTC causes a shift in the binding energy peaks of Bi $4f_{5/2}$ and Bi $4f_{7/2}$ to 159.8 eV and 165.1 eV, respectively. However, the ΔE between Bi

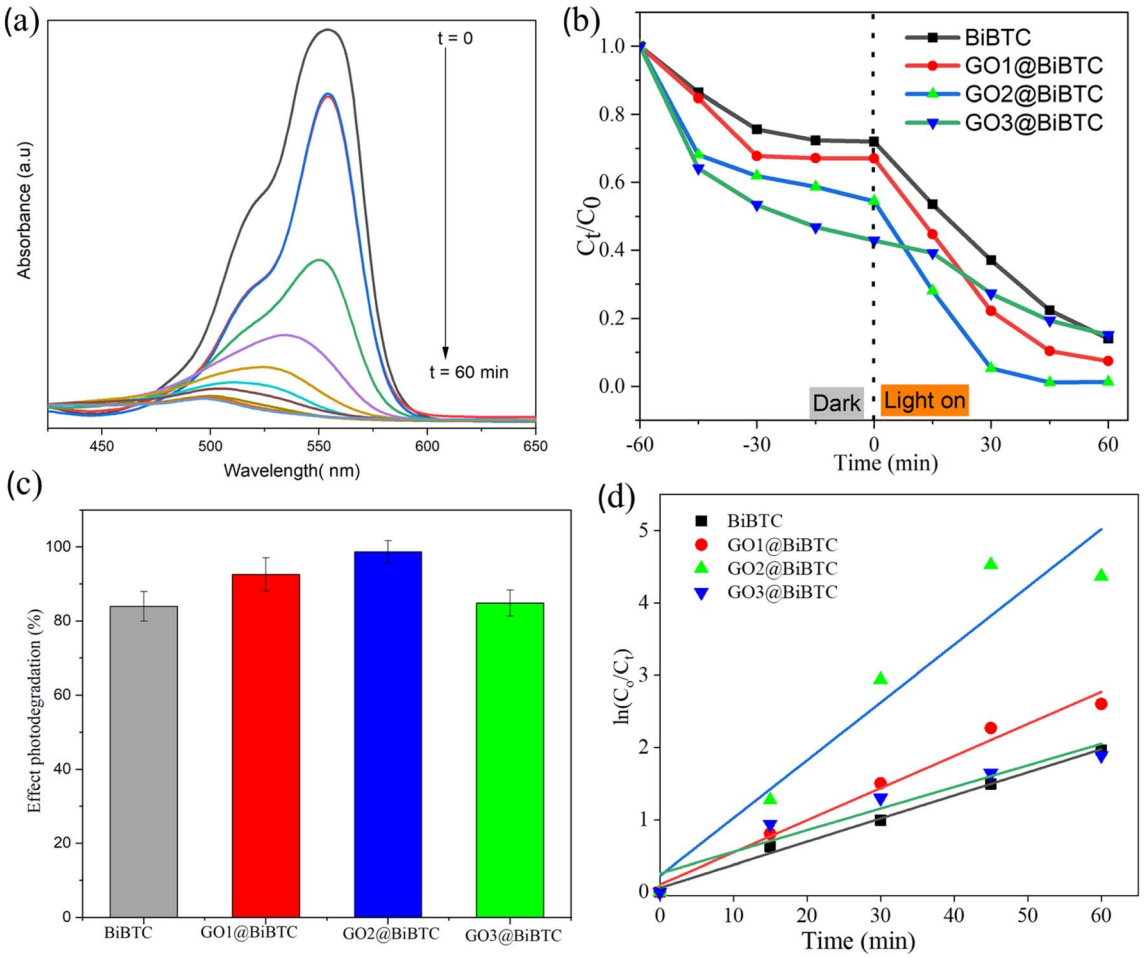

Fig. 12 (a) Absorbance drops under light irradiation, (b) C/C_0 *vs.* irradiation time plots, (c) effect photodegradation-dependent discolorations, and (d) $\ln(C_0/C)$ *vs.* irradiation time curves using the as-synthesized samples.

$4f_{5/2}$ and Bi $4f_{7/2}$ for GO@BiBTC remains unchanged compared to BiBTC (Fig. 10c). These results indicate that the Bi element primarily exists in the form of Bi(III).

The results in Fig. 11 show that the GO2@BiBTC composite exhibited a smaller Nyquist radius compared to BiBTC, indicating that the charge separation and transfer of GO2@BiBTC are more efficient than those of BiBTC. This implies an improved charge transfer efficiency, leading to enhanced photocatalytic performance.

Photocatalytic performance

As illustrated in Fig. 12a, the real-time concentration of organic dye after 60 min irradiation *versus* the initial dye concentration was derived from the absorbance measured at the RhB's characteristic light-absorption wavelength (553 nm). After 60 min of light illumination, BiBTC sample displayed only 80% degradation of RhB whereas GO2@BiBTC MOF and GO3@BiBTC MOF showed more than 90% degradation. The synthesized GO2@BiBTC MOF revealed the maximal deterioration rate (98%) among four catalysts under the same condition (Fig. 12b and c).

The photodegradation reaction fits the pseudo-first-order kinetics well, as shown in Fig. 12d. The apparent deterioration rate constants (k) value of BiBTC, GO1@BiBTC MOF, GO2@BiBTC MOF, GO3@BiBTC MOF composites were 0.03, 0.04, 0.07 and 0.02 min^{-1}, respectively. The finding

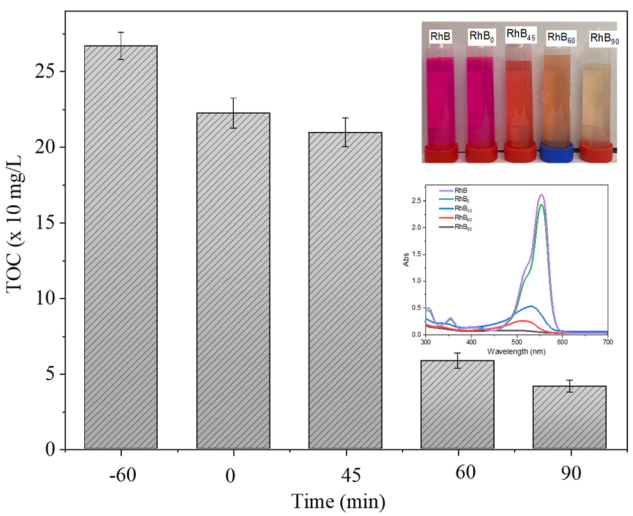

Fig. 13 Total organic carbon (TOC) removal during the photocatalytic degradation of RhB in the presence of GO@BiBTC.

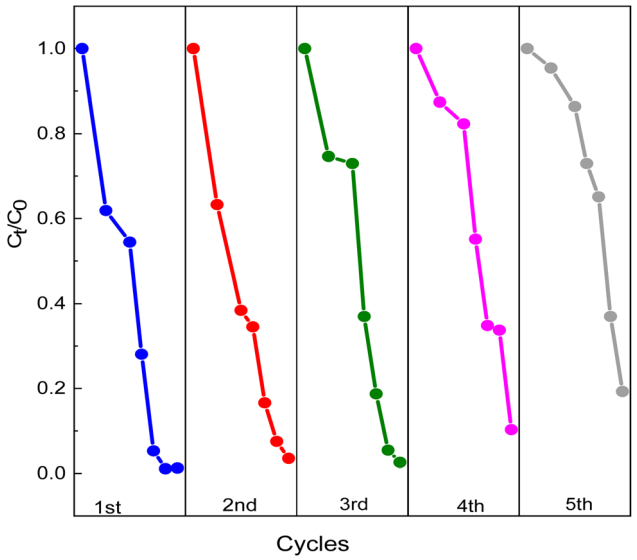

Fig. 14 Cyclic photocatalytic degradation RhB degradation.

displayed that the optimized heterostructure illustrated the maximal photocatalytic performance, which was clearly owing to the combination effect of BiBTC and GO. The stability and reproducibility of the sample are crucial factors in the field of wastewater treatment.

The total organic carbon (TOC) removal efficiency of RhB by GO@BiBTC was determined according to the ISO 8245:1999 standard using a TOC-VCPH analyzer from Shimadzu. The results show a significant reduction in TOC removal efficiency with increasing reaction time (Fig. 13). TOC removal efficiency reached by 78.5% and 84.5% after reaction times of 60 and 90 min, respectively.

Fig. 14 illustrates the photodegradation activity of RhB using GO2@BiBTC MOF composite after five runs. The removal rate of GO2@BiBTC MOF heterostructure was cyclically used at about 90% after 4th run, ascribing good stability and reproducibility of the optimized catalyst. The FT-IR and XRD spectra of the GO2@BiBTC MOF composite after five catalytic cycles remained comparable to those of the fresh material, with only a slight reduction in peak intensities (Fig. 15a and b). Similarly, SEM analysis revealed minimal morphological changes in the

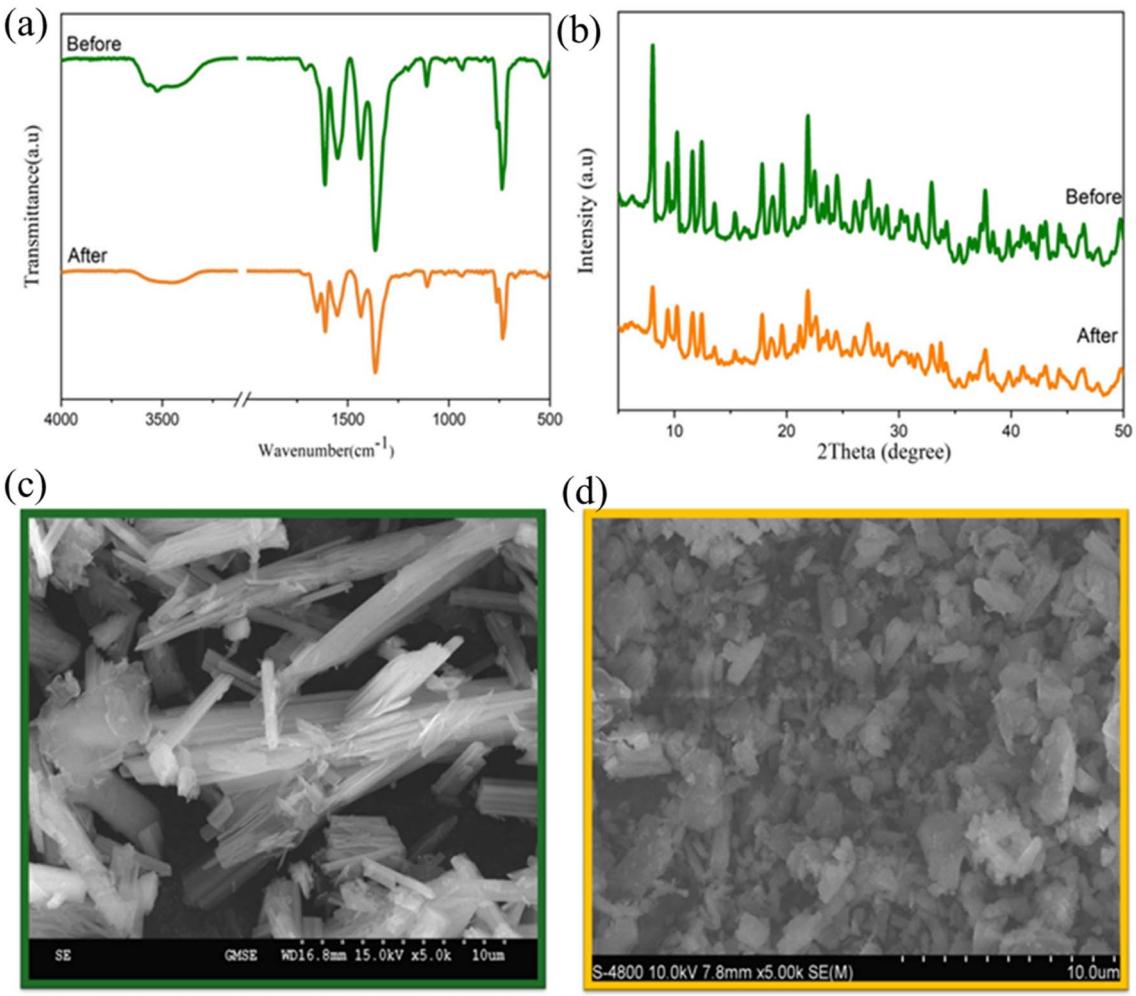

Fig. 15 (a) FT-IR, (b) XRD patterns, SEM image of GO2@BiBTC MOF catalyst (c) before and (d) after the cycling test.

Table 1 Comparison of the photocatalytic efficiency of RhB dye degradation using GO2@BiBTC MOF with findings from previous studies

Catalyst	Catalyst amount (mg)	RhB concentration (mg mL^{-1})	Reaction time (min)	Light source	Degradation efficiency (%)	Ref.
MIL-88A(Fe)/GO–H_2O_2	20	10	80	Xenon lamp	100	49
GO/MIL-53(Fe)–H_2O_2	10	20		Xenon lamp	100	50
MIL-88(Fe)@GO	5	100	60	Natural sunlight	98	51
Nd-MOF/GO/Fe_3O_4	2	10	80	Sunlight	20	52
$BiVO_4$/MIL-Fe/GO	10	15	30	Visible light	78	53
GO@BiBTC MOF	10	15	60	LED light	98	This work

composite due to some BiBTC rods exhibited breakage during the reaction process (Fig. 15c and d). Overall, these results confirm the catalyst's robust stability.

Table 1 compares the photocatalytic efficacy of our GO2@BiBTC MOF composite in degrading RhB with a state-of-the-art heterostructure documented in prior literature. While our photocatalyst did not exhibit superior degradation compared to other composites, it represents a promising candidate for enhancing and integrating efficient photocatalysts for water purification purposes.

Photocatalytic mechanism

The free radical ($^{\bullet}OH$, $^{\bullet}O_2^-$, h^+, and e^-) trapping measurements were analyzed to confirm the radicals involved in the photocatalytic process over GO2@BiBTC MOF catalyst. TBA was utilized as the quencher of $^{\bullet}OH$, BQ ($^{\bullet}O_2^-$), $K_2Cr_2O_7$ (e^-), $Na_2C_2O_4$ (h^+), respectively. In brief, their effect on the RhB deterioration efficiency of composite is demonstrated in Fig. 16a. It is obvious that GO2@BiBTC MOF catalyst has shown well to degrade 98% RhB in 60 min without scavenger molecules. However, the deterioration rate of RhB has fallen to 98%, 90%, 34%, and 29% respectively for TBA, $K_2Cr_2O_7$, BQ, and $Na_2C_2O_4$ upon the addition of scavengers. These results clearly reveal the major contribution from $^{\bullet}O_2^-$ and h^+ as dominant reactive oxygen species in the whole process. Moreover, e^- and $^{\bullet}OH$ species are found to participate in the photocatalytic degradation of RhB.

The schematic presentation of the improvement adsorption-photodegradation mechanism of RhB under light irradiation is displayed in Fig. 16b. The adsorption of RhB onto Bi–GO composite happened by both van der Waals forces and porosity structure with a large specific surface area, which was investigated in previous reports.[27,41–43] Moreover, under light illumination, GO@BiBTC MOF photocatalyst generates electrons and holes in the conduction band and valence band, which will react with water molecules and oxygen to create super radicals like OH^- and $^{\bullet}O_2^-$. These reactive radicals tend to transform RhB into intermediate products and by-products (CO_2 + H_2O), as shown below.

$$\text{GO@BiBTC MOF} + h\nu \rightarrow e^- + h^+$$

$$O_2 + e^- \rightarrow {}^{\bullet}O_2^-$$

$$h^+ + H_2O \rightarrow {}^{\bullet}OH$$

$$h^+/{}^{\bullet}O_2^- + {}^{\bullet}OH + \text{RhB} \rightarrow CO_2 + H_2O$$

Additionally, the likely intermediates during the photocatalytic reaction were identified using LC-MS/MS spectroscopy.

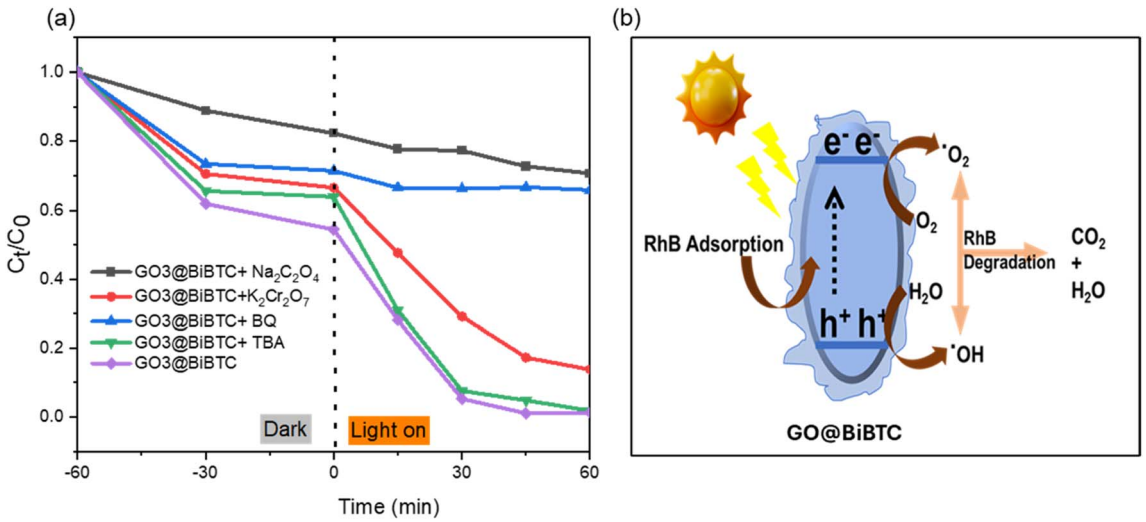

Fig. 16 (a) Photocatalytic RhB degradation RhB degradation without and with radical scavengers and (b) the removal mechanism of RhB by GO@BiBTC MOF heterostructure.

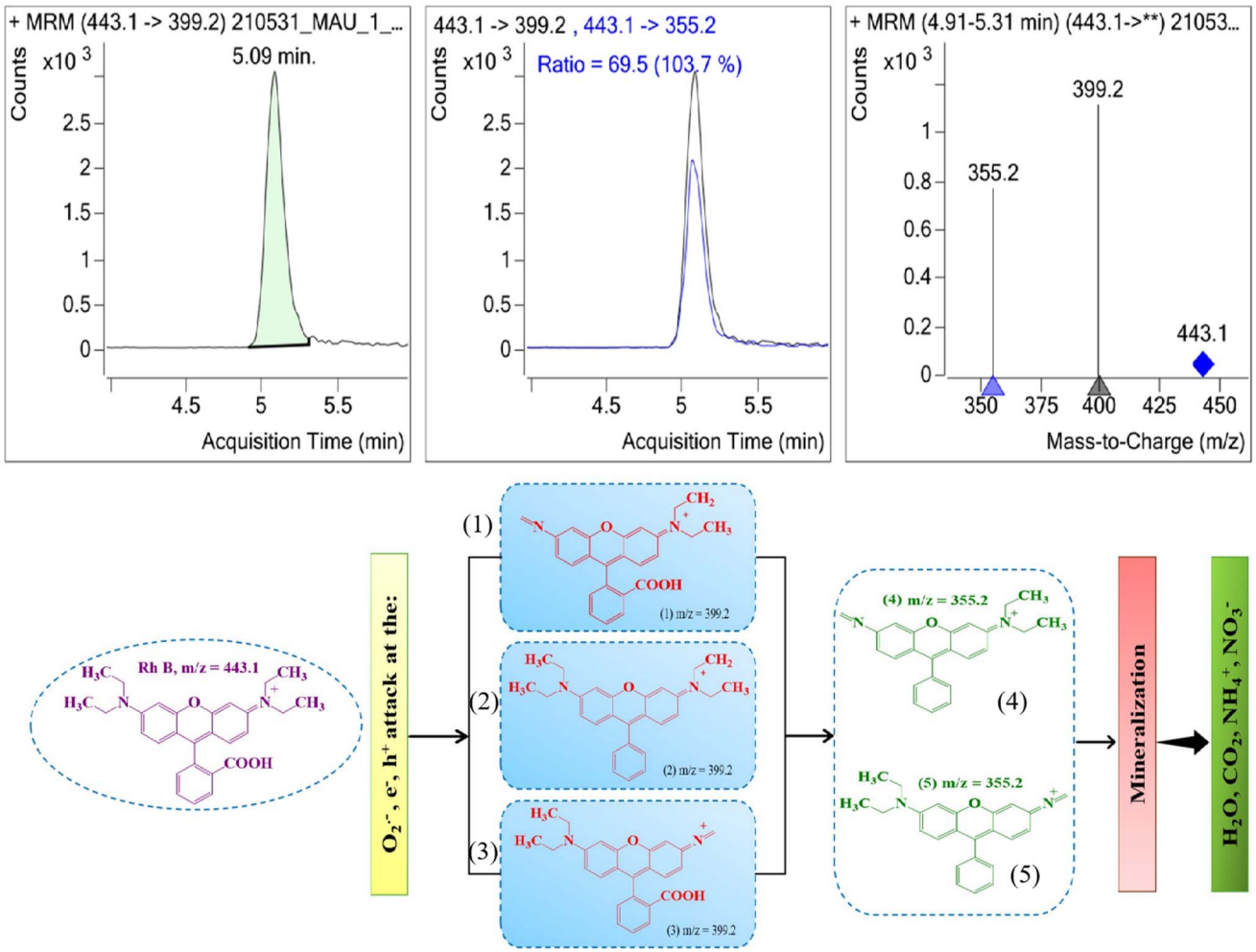

Fig. 17 LC-MS/MS spectroscopy and schematic diagram of plausible degradation of RhB using GO@BiBTC MOF catalyst.

A suggested photodegradation route for RhB was derived from spectrum measurements (Fig. 17). The initial RhB had an *m*/*z* value of 399.2, corresponding to formulae (1)–(3). The intermediate products were associated with formulae (4) and (5) and had a *m*/*z* value of 355.2. Additionally, primary oxidation products were produced and subsequently degraded into smaller molecules. Following that, the oxidizing intermediates broke down into CO_2, NO_3^-, NH_4^+, and H_2O.[54–57]

Conclusion

In this study, a binary GO@BiBTC MOF heterostructure was successfully synthesized *via* hydrothermal technique. In comparison with pristine BiBTC, the binary composite displayed improved adsorption-photocatalytic performance (98%) than BiBTC towards RhB degradation. The free active species trapping experiments revealed that the superspecies h^+ and $^{\cdot}O_2^-$ were the major reactive species in the adsorption-photocatalytic degradation course, to achieve RhB degradation. This work provided a new strategy to synthesize effective binary GO@BiBTC MOF heterostructure composites and facilitate the field of wastewater treatment.

Data availability

Data supporting this article are available upon the request from corresponding authors.

Author contributions

Van Cuong Nguyen: writing – review and editing; investigation; visualization, supervision; Trinh Duy Nguyen: conceptualization; validation; Qui Thanh Hoai Ta: writing – original draft, formal analysis; Ai Le Hoang Pham: conceptualization, investigation, methodology, formal analysis.

Conflicts of interest

There are no conflicts to declare.

Acknowledgements

This research is supported by Industrial University of Ho Chi Minh City (IUH) under grant number 105/HD-DHCN.

References

1 S. Mosleh, K. Dashtian, M. Ghaedi and M. Amiri, *RSC Adv.*, 2019, **9**, 30100–30111.
2 K. S. Varma, R. J. Tayade, K. J. Shah, P. A. Joshi, A. D. Shukla and V. G. Gandhi, *Water-Energy Nexus*, 2020, **3**, 46–61.
3 U. G. Akpan and B. H. Hameed, *J. Hazard. Mater.*, 2009, **170**, 520–529.
4 Q. T. H. Ta, E. Cho, A. Sreedhar and J.-S. Noh, *J. Catal.*, 2019, **371**, 1–9.
5 J. Luo, P. Lin, P. Zheng, X. Zhou, X. Ning, L. Zhan, Z. Wu, X. Liu and X. Zhou, *Chemosphere*, 2022, **298**, 134297.
6 S. Sharma, V. Dutta, P. Raizada, A. Hosseini-Bandegharaei, V. K. Thakur, A. Singh, Q. Van Le, V.-H. Nguyen and P. Singh, *Mater. Lett.*, 2021, **297**, 129940.
7 S. Gautam, H. Agrawal, M. Thakur, A. Akbari, H. Sharda, R. Kaur and M. Amini, *J. Environ. Chem. Eng.*, 2020, **8**, 103726.
8 G. Cai, P. Yan, L. Zhang, H.-C. Zhou and H.-L. Jiang, *Chem. Rev.*, 2021, **121**, 12278–12326.
9 Y. Wen, P. Zhang, V. K. Sharma, X. Ma and H.-C. Zhou, *Cell Rep. Phys. Sci.*, 2021, **2**, 100348.
10 Z. Li, G. Huang, K. Liu, X. Tang, Q. Peng, J. Huang, M. Ao and G. Zhang, *J. Cleaner Prod.*, 2020, **272**, 122892.
11 Y. Tang, H. Kang, J. Zheng, H. Li, R. Wang, L. Zhang, Q. Ma, X. Xiong, T. Zhou, C. Zhang and J. Power, *Sources*, 2022, **520**, 230895.
12 H. Qin, Y. Lv, P. Li, M. Xiao, H. Song, Q. Zhang and J. Yang, *New J. Chem.*, 2021, **45**, 21888–21895.
13 F. Li, G. H. Gu, C. Choi, P. Kolla, S. Hong, T.-S. Wu, Y.-L. Soo, J. Masa, S. Mukerjee and Y. Jung, *Appl. Catal., B*, 2020, **277**, 119241.
14 A. K. Inge, M. Köppen, J. Su, M. Feyand, H. Xu, X. Zou, M. O'Keeffe and N. Stock, *J. Am. Chem. Soc.*, 2016, **138**, 1970–1976.
15 W. Chai, W. Yin, K. Wang, W. Ye, B. Tang and Y. Rui, *Electrochim. Acta*, 2019, **325**, 134927.
16 M. Åhlén, E. Kapaca, D. Hedbom, T. Willhammar, M. Strømme and O. Cheung, *Microporous Mesoporous Mater.*, 2022, **329**, 111548.
17 L. Stobinski, B. Lesiak, A. Malolepszy, M. Mazurkiewicz, B. Mierzwa, J. Zemek, P. Jiricek and I. Bieloshapka, *J. Electron Spectrosc. Relat. Phenom.*, 2014, **195**, 145–154.
18 S. N. Alam, N. Sharma and L. Kumar, *Graphene*, 2017, **6**, 1–18.
19 D. A. Dikin, S. Stankovich, E. J. Zimney, R. D. Piner, G. H. B. Dommett, G. Evmenenko, S. T. Nguyen and R. S. Ruoff, *Nature*, 2007, **448**, 457.
20 G. F. Smaisim, A. M. Abed, H. Al-Madhhachi, S. K. Hadrawi, H. M. M. Al-Khateeb and E. Kianfar, *Bionanoscience*, 2023, **13**, 219–248.
21 K. A. U. Madhushani, A. Perera, A. Kumar and R. K. Gupta, *Inorg. Chem. Commun.*, 2023, 111446.
22 K. Kim, H. Jung and K. M. Cho, *ACS Appl. Mater. Interfaces*, 2023, **15**, 41755–41762.
23 R. Majidi, I. Danaee, L. Vrsalović and D. Zarei, *Mater. Chem. Phys.*, 2023, **308**, 128291.
24 M.-L. Xu, X.-J. Jiang, J.-R. Li, F.-J. Wang, K. Li and X. Cheng, *ACS Appl. Mater. Interfaces*, 2021, **13**, 56171–56180.
25 N. D. Kolhe, L. S. Walekar, A. N. Kadam, A. S. Chopade, S.-W. Lee, D. S. Mhamane, S. N. Shringare, A. S. Lawand, G. S. Gokavi and M. Misra, *J. Cleaner Prod.*, 2023, **420**, 138179.
26 S. Yin, Y. Chen, C. Gao, Q. Hu, M. Li, Y. Ding, J. Di, J. Xia and H. Li, *J. Photochem. Photobiol., A*, 2020, **387**, 112149.
27 M. B. Nguyen, G. H. Le, T. D. Nguyen, Q. K. Nguyen, T. T. T. Pham, T. Lee and T. A. Vu, *J. Hazard. Mater.*, 2021, **420**, 126560.
28 H. T. Vu, M. B. Nguyen, T. M. Vu, G. H. Le, T. T. T. Pham, T. D. Nguyen and T. A. Vu, *Top. Catal.*, 2020, **63**, 1046–1055.
29 R. Rathinam, M. Govindaraj, K. Vijayakumar and S. Pattabhi, *Desalin. Water Treat.*, 2016, **57**, 16995–17001.
30 J. Sharma, S. Sharma, U. Bhatt and V. Soni, *J. Hazard. Mater. Lett.*, 2022, **3**, 100069.
31 Y. Zhao, X. Fan, H. Zheng, E. Liu, J. Fan and X. Wang, *J. Mater. Sci. Technol.*, 2024, **170**, 200–211.
32 Q. T. H. Ta, N. M. Tran and J.-S. Noh, *Catalysts*, 2020, **10**, 1140.
33 K. Ahmad, H. R. Ghatak and S. M. Ahuja, *Environ. Technol. Innovation*, 2020, **19**, 100893.
34 H. A. Le Pham, D. T. Nguyen, V. C. Nguyen and T. K. Vo, *Inorg. Chem. Commun.*, 2024, **159**, 111822.
35 S.-R. Zhu, M.-K. Wu, W.-N. Zhao, P.-F. Liu, F.-Y. Yi, G.-C. Li, K. Tao and L. Han, *Cryst. Growth Des.*, 2017, **17**, 2309–2313.
36 H. Qu, L. Huang, Z. Han, Y. Wang, Z. Zhang, Y. Wang, Q. Chang, N. Wei, M. J. Kipper and J. Tang, *J. Porous Mater.*, 2021, **28**, 1837–1865.
37 D. C. Marcano, D. V. Kosynkin, J. M. Berlin, A. Sinitskii, Z. Sun, A. Slesarev, L. B. Alemany, W. Lu and J. M. Tour, *ACS Nano*, 2010, **4**, 4806–4814.
38 H. A. Le Pham, A. A. Abd, T. H. A. Nguyen, N. B. T. Le, T. D. Nguyen, V. C. Nguyen and M. R. Othman, *Chem. Eng. Res. Des.*, 2023, **198**, 196–207.
39 Q. Zhang, Y. Lei, L. Li, J. Lei, M. Hu, T. Deng, Y. Zhang and P. Ma, *Sustainable Chem. Pharm.*, 2023, **33**, 101038.
40 X. Jiao, Y. Qiu, L. Zhang and X. Zhang, *RSC Adv.*, 2017, **7**, 52337–52344.
41 S. Li, Q. Zhang, H. Deng, S. Chen, X. Shen, Y. Yuan, Y. Cheng, J. Zhu and B. Lu, *Small Methods*, 2023, **7**, 2201554.
42 D. Yao, C. Tang, A. Vasileff, X. Zhi, Y. Jiao and S. Qiao, *Angew. Chem.*, 2021, **133**, 18326–18332.
43 X. Yue, L. Cheng, F. Li, J. Fan and Q. Xiang, *Angew. Chem.*, 2022, **134**, e202208414.
44 M. Jain, D. Mishra, S. A. Khan, K. K. Pant, Z. M. Ziora and M. A. T. Blaskovich, *J. Chem. Eng.*, 2024, 151351.
45 C. Chen, L. Fei, B. Wang, J. Xu, B. Li, L. Shen and H. Lin, *Small*, 2024, **20**, 2305066.
46 Y. Zhang, X. Yu, Y. Hou, C. Liu, G. Xie and X. Chen, *Mol. Catal.*, 2024, **555**, 113851.
47 P. Makuła, M. Pacia and W. Macyk, *J. Phys. Chem. Lett.*, 2018, **9**, 6814–6817.

48 A. E. Hassan, A. M. Elewa, M. S. A. Hussien, A. F. M. EL-Mahdy, I. M. A. Mekhemer, I. S. Yahia, T. A. Mohamed, H.-H. Chou and Z. Wen, *J. Colloid Interface Sci.*, 2024, **653**, 1650–1661.
49 N. Liu, W. Huang, X. Zhang, L. Tang, L. Wang, Y. Wang and M. Wu, *Appl. Catal., B*, 2018, **221**, 119–128.
50 C. Zhang, L. Ai and J. Jiang, *Ind. Eng. Chem. Res.*, 2015, **54**, 153–163.
51 Y. Wu, H. Luo and H. Wang, *RSC Adv.*, 2014, **4**, 40435–40438.
52 Y. Bai, S. Zhang, S. Feng, M. Zhu and S. Ma, *Dalton Trans.*, 2020, **49**, 10745–10754.
53 Y. Chen, B. Zhai and Y. Liang, *Diamond Relat. Mater.*, 2019, **98**, 107508.
54 M. Zhang, H. Yin, J. Yao, M. Arif, B. Qiu, P. Li and X. Liu, *Colloids Surf., A*, 2020, **602**, 124778.
55 X. Zheng, D. Li, X. Li, L. Yu, P. Wang, X. Zhang, J. Fang, Y. Shao and Y. Zheng, *Phys. Chem. Chem. Phys.*, 2014, **16**, 15299–15306.
56 T.-L. T. Le, T.-H. T. Le, H. T. Huu, D. T. T. Nu, L. N. Thi, T. T. T. Phan, K. N. Van, P. H. Nguyen and V. Vo, *J. Alloys Compd.*, 2024, 174716.
57 S. Hisaindee, M. A. Meetani and M. A. Rauf, *TrAC, Trends Anal. Chem.*, 2013, **49**, 31–44.